PS imaging of ocean-bottom data

Lorenzo Casasanta[1] and Samuel H. Gray[1]

Abstract

Opportunities and challenges exist for imaging seismic data acquired using conventional marine sources and receivers on the seafloor. Compared with conventional imaging of sea-surface streamer data, seabed acquisition and processing offer some opportunities to provide higher value of information. One of the opportunities is to use P-wave to S-wave converted reflection energy (PS imaging). Challenges include overcoming the effects of current seafloor receiver spacing, which can be large enough to negate the promised resolution gains and complicate the velocity model-building workflow. A synthetic data set illustrates possible imaging improvements that can result from seafloor acquisition as well as image degradation that can result when seafloor receivers are separated by typical current distances.

Introduction

Seismic data acquisition using acoustic sources near the sea surface and multicomponent receivers at the seafloor offers some advantages over conventional towed-streamer acquisition. Placing receivers on the seafloor can result in improved imaging in the presence of obstructions such as drilling platforms, full-azimuth acquisition, improved multiple imaging and suppression, and wider seismic bandwidth. Seafloor acquisition also allows the imaging of seismic energy converted from P-wave to S-wave at subsurface reflection points.

Such PS, or converted-wave, imaging can complement and add value to conventional PP imaging, which uses receivers either near the sea surface or at the seafloor. Low S-wave velocities relative to P-wave velocities result in shorter S-wavelengths and the potential for higher resolution in PS images than in PP images.

Furthermore, PS reflectivity is generally different from PP reflectivity. PP reflected amplitudes depend on different rock- and fluid-property contrasts from PS-reflected amplitudes. This extra information allows for more stable and reliable elastic rock-property inversions than information from P-waves alone. In addition, shear-wave splitting analysis can provide information about fracture orientation in the subsurface. Finally, PS reflections have proved useful in imaging through gas clouds, which attenuate P-wave energy. See Stewart et al. (2003) for a review of PS seismic-exploration applications.

On the other hand, seafloor acquisition can cause serious problems for PS imaging. These are usually related to receiver spacing, either the crossline distance between ocean-bottom cables (OBC) or the inline and crossline distances between ocean-bottom nodes (OBN). The large receiver spacing used in current seafloor acquisitions is problematic for PS imaging and can negate any potential for improved spatial resolution. Inline or crossline separations greater than an S-wavelength compromise the ability to image just below the seafloor using S-waves, especially between cables or nodes.

For PP imaging, this problem can be solved to a large degree by mirror imaging (Dash et al., 2009), in which the sea surface acts as a mirror. The mirror reflects upgoing primary P-waves, and the downgoing P-waves recorded at the seafloor are treated as primary energy recorded at a fictitious reversed image of the seafloor placed above the sea surface (Figure 1). The migration aperture, or illumination cone, from locations on the fictitious recording surface is wider than that from the actual recording surface (the seafloor), resulting in a more complete shallow PP image.

For PS imaging, no S-wave energy transmits upward in the water column to be reflected at the sea surface, so PS mirror imaging is not available. Further, the S-wave illumination cone is always much more restricted in angle than the P-wave illumination cone because the lower S-wave velocity tends to turn reflected energy nearly vertical at the receiver locations (Figure 1).

These difficulties reduce the value that PS imaging adds to PP imaging, but they do not cancel it completely. Despite them, we observe some of the promised uplift of PS imaging, and we see clear potential for the technology.

We illustrate the present state of the art of PS imaging on a synthetic anisotropic, viscoelastic seafloor 2D data set that has relatively fine receiver spacing. This simulates 2D OBC data. We decimate receivers to simulate OBN data and investigate the problems that arise from large receiver spacing. We compare PP and PS images of the fully sampled and decimated data sets to show the relative benefits of PP and PS imaging, paying special attention to the improved resolution that is possible in PS imaging.

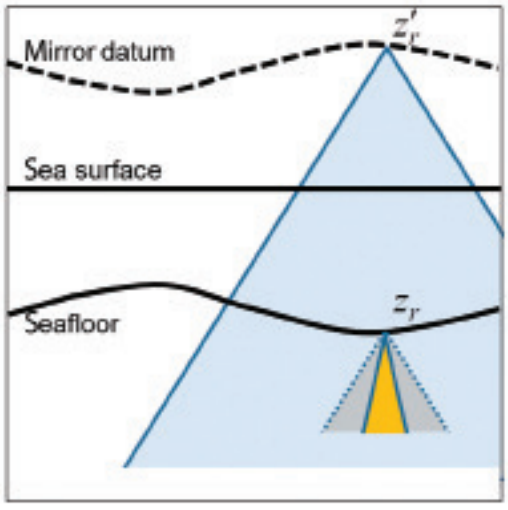

Figure 1. Principle of mirror migration of downgoing P-waves. The downgoing travel path is mirrored at the sea surface. Moving the receiver location from the seafloor to its mirrored location results in an expanded illumination cross section at the seafloor (from the gray cone to the light blue one). The yellow cone depicts the narrower S-wave illumination cross section. The low S-wave velocity typically forces the PS-wavefield to emerge nearly vertically at the receiver locations.

[1]CGG.

http://dx.doi.org/10.1190/tle34040414.1.

We also show common-image gathers (CIG) from the various migrations, indexed by the subsurface incidence angle or the dip angle, and we discuss the relative benefits and drawbacks of these for migration amplitude analysis and, in particular, velocity model building.

PP and PS image comparisons

Our test data set models 2D acquisition in a deepwater setting, with P-wave sources and combined hydrophone/geophone receivers recording P-wave energy and horizontal and vertical components of particle motion. The line is approximately 17 km long, with 170 seafloor receivers placed 100 m apart and 1280 sources placed 12.5 m apart. Both structure and stratigraphy are complex and velocity contrasts are significant, with P-wave velocities V_P ranging from water velocity to approximately 5000 m/s and S-wave velocities V_S as low as 300 m/s.

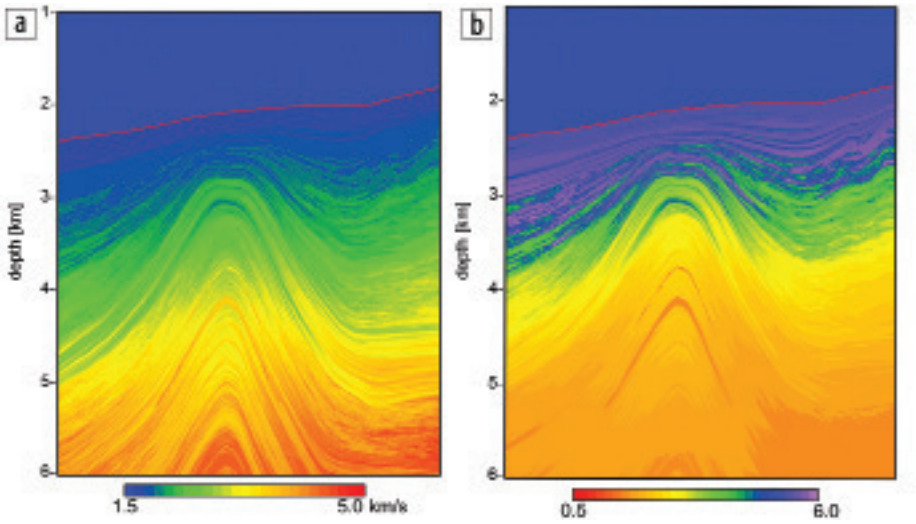

Figure 2. Velocity fields for synthetic data set: (a) P-wave velocity; (b) ratio of P-wave velocity to S-wave velocity.

Figure 2 shows the P-wave velocity field (Figure 2a) and the V_P/V_S ratio (Figure 2b). The model is attenuative and anisotropic, with tilted polar anisotropy that is not conformable with layering of velocity. We performed common-receiver beam migration to produce all the images. We used Gaussian-beam migration (GBM) (Hill, 2001), motivated by its increased accuracy over Kirchhoff migration and its increased efficiency over reverse time migration (RTM).

An additional advantage of beam migration over RTM is the handling of S-wave anisotropy, which can cause problems for RTM. A standard method for dealing with S-wave anisotropy in RTM is limited to weak anisotropy. The presence of strong anisotropy can cause cusped S-wavefields even in homogeneous media, which the strong formulation allows but the weak formulation does not (Casasanta and Gray, 2015). Therefore, standard weak-anisotropy S-wave RTM extrapolators can be kinematically inaccurate, whereas beam migration can use the strong anisotropy formulation.

Beam migration, like Kirchhoff migration, can include operator antialiasing (Gray, 2013), but we chose not to antialias the operator for any of the migrations. This allowed us to observe "worst-case" effects of receiver sampling in all our images and CIGs. Because of the fine source spacing, neither common-receiver PP migrations nor common-receiver PS migrations suffered individually from operator aliasing. Therefore, the only migration aliasing effects came from combining individual images, either summing them to view final stacks or interleaving them to form CIGs.

Our baseline image (Figure 3a) used as input the upgoing PP wavefield with 100-m receiver spacing (simulated OBC acquisition). Its overall wide bandwidth results from the separation of the upgoing and downgoing pressure wavefields, followed by their spectral division. This so-called up-down deconvolution (Amundsen, 2001) guarantees ideal source designature and complete surface-related multiple removal for a horizontally layered earth.

Wang et al. (2010) demonstrate the robustness and success of up-down deconvolution even in the presence of complex geology and with a mildly dipping sea bottom, as in our example. Consequently, Figure 3a shows good structural imaging as well as stratigraphic details in the layers draped over the anticline in the center of the section. There is fine layering just below the seafloor. A PP migration that accounted for attenuation (not illustrated) showed little improvement in near-surface resolution. The stack also shows some effects of migration aliasing in the shallow section.

The aliasing becomes more evident in Figure 3b, where receiver spacing has been increased to 300 m (simulated OBN acquisition). Aliased migration swings interfere with the interpretability of shallow events and call into doubt the interpretability of the stratigraphic section. The effects of large receiver spacing are also evident deeper in the section in Figure 3b, although the noise at depth has a less coherent appearance than the shallow noise does.

PS images corresponding to the PP images in Figures 3a and 3b are shown in Figures 3c and 3d — 100-m receiver spacing in Figure 3c and 300-m receiver spacing in Figure 3d. Using the analogue of up-down deconvolution for horizontal recording, the "radial component" (in this 2D case, the single horizontal component) has been deconvolved by the downgoing pressure wavefield in an effort to eliminate any P-wave surface-related multiples leaking on the horizontal geophone recording.

Both PS images appear to be more corrupted by aliasing noise than the PP images are. This is partly because of the nature of PS reflection. Because of its polarity flip at zero reflection angles (Rosales and Rickett, 2001), unmigrated PS data have diminished amplitudes on near-offset horizontal events relative to steep reflection events. Therefore, PS-migrated amplitudes will tend to be greater on steep events, exaggerating the effects of migration aliasing.

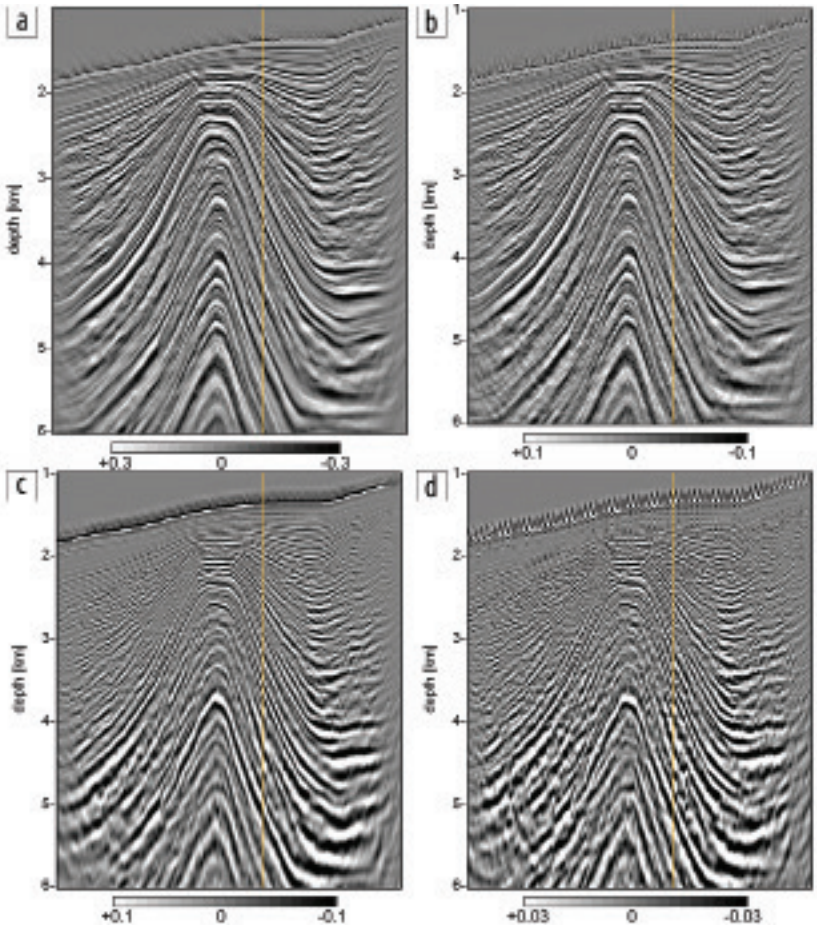

Figure 3. OBN 2D synthetic stacked sections after (a and b) PP-wave and (c and d) PS-wave migration, with receiver spacing of (a and c) 100 m and (b and d) 300 m. As expected, the stack amplitudes in (b) and (d) are three times less than those in (a) and (c) because of node decimation.

Although the PS images are noisy, the PS seismic wavelet has a noticeably smaller wavelength (Figures 3c and 3d) in the layering just below the seafloor than the corresponding PP images (Figures 3a and 3b), fulfilling to some degree the promise of high resolution of PS images. On the other hand, although vertical resolution is visibly higher in the PS images than in the PP images, lateral resolution is visibly lower.

As indicated in Figure 1, the illumination cones of PS migration are narrower than those of PP migration, leaving gaps in the image that persist to large depths below the seafloor. The possibility of delineating lateral terminations of fine-scale features is therefore diminished, especially for OBN data (Figure 3d).

In addition, spatial resolution deeper in the section is greater for PP than for PS. This is because of the greater effect of attenuation on S-wave propagation than on P-wave propagation over comparable distances. A PS migration that accounted for attenuation improved deep resolution but did not provide resolution to match the baseline PP image. This migration was unable to recover all the energy that was attenuated during S-wave propagation.

PP and PS CIG comparisons

Using the same test data set, we present and compare different types of CIGs from upgoing PP and PS seismic-wavefield migrations. These gathers are evaluated on the right side of the survey, where the seafloor is nearly flat. We sampled seven CIGs centered at the location indicated by the yellow line in Figure 3 and spaced at 100 m. For the simulated OBN survey (300-m node spacing), the first, fourth, and seventh CIG locations (Figures 5b, 5d, 6b, and 6d below) coincide with node locations. This particular choice lets us evaluate the effect of coarse sampling on CIGs between node locations.

CIGs indexed by surface coordinates are used routinely in seismic processing and imaging. The most familiar type of CIG is indexed by offset. For data recorded with separate datum surfaces for sources and receivers, *offset* means lateral offset between source and receiver locations. These gathers are used for tomographic velocity analysis in which, for seafloor recording, tomography must account for separate datum surfaces just as migration does. In complex geology, strong velocity contrasts can cause wave-propagation multipathing, which manifests itself as artifacts in image gathers indexed by any surface coordinate (Xu et al., 2001).

For this reason, we expect CIGs indexed by the subsurface incidence angle to be more accurate and reliable for tomography and amplitude analysis than surface-offset CIGs are. In our chosen example, wave propagation is relatively well behaved. Therefore, the CIGs that are indexed by incidence-angle-indexed CIGs tell essentially the same story as the offset-indexed CIGs. In fact, they resemble horizontally stretched (shallow) and squeezed (deep) versions of offset-indexed CIGs, with the added feature of allowing amplitude-variation-with-angle (AVA) analysis instead of the less desirable amplitude-variation-with-offset (AVO) analysis. Because our observations about offset- and incidence-angle-indexed CIGs are similar, we discuss only the latter in the following.

In Gaussian-beam migration, incident and reflected wave directions are kept during the imaging process and can be used to compute both the migration dip angle and the incidence angle while imaging (Gray, 2007). This allows migrated energy to be partitioned into traces with nominal (binned) incidence angles or dip angles, i.e., into incidence- or dip-angle CIGs. The simplicity of extracting GBM angle gathers makes them attractive in comparison with the relatively complicated computation of RTM angle gathers.

For PP migration, the subsurface incidence angle is one-half the difference between source and receiver angles in the plane of reflection, and the dip angle is the average of the two angles. This is not the case for PS migration, for which both incidence angle and dip angle must be computed from Snell's law using

local values for P-wave and S-wave velocity. We show incidence-angle gathers for PP and PS in Figure 4, with an incidence-angle range of –60° to 60° and a 6°-angle bin sampling.

From Figure 4, the CIGs obtained from migrating the upgoing PP wavefield (Figure 4a) are cleaner and overall more diagnostic of slight velocity errors than the corresponding PS gathers (Figure 4c). On the other hand, the PS gathers show greater vertical resolution just below the receiver locations. In addition, the PS gathers show weak reflection energy near polarity transitions of the PS data, which usually occur near zero offset or incidence angle.

The PP gathers with 300-m receiver spacing (Figure 4b) show distinct upward-curving events just below the seafloor and discontinuities in events at shallow depths. These are migration aliasing effects, which are spread over a large range by the wide illumination cones of the PP migration operator and result in incomplete summation.

These events do not appear on the shallow PS gathers because the narrow PS illumination cones prevent the tails of the migration operator from spreading from one receiver location to the next. In the shallow sediments near each node, we see in effect the result of a single receiver-wavefield migration, which is unaliased because the data are well sampled. At the same time, however, the narrow PS cones prevent more than a few receivers from "seeing" any near-seafloor location, and this reduces the effectiveness of PS CIGs for between-node velocity discrimination.

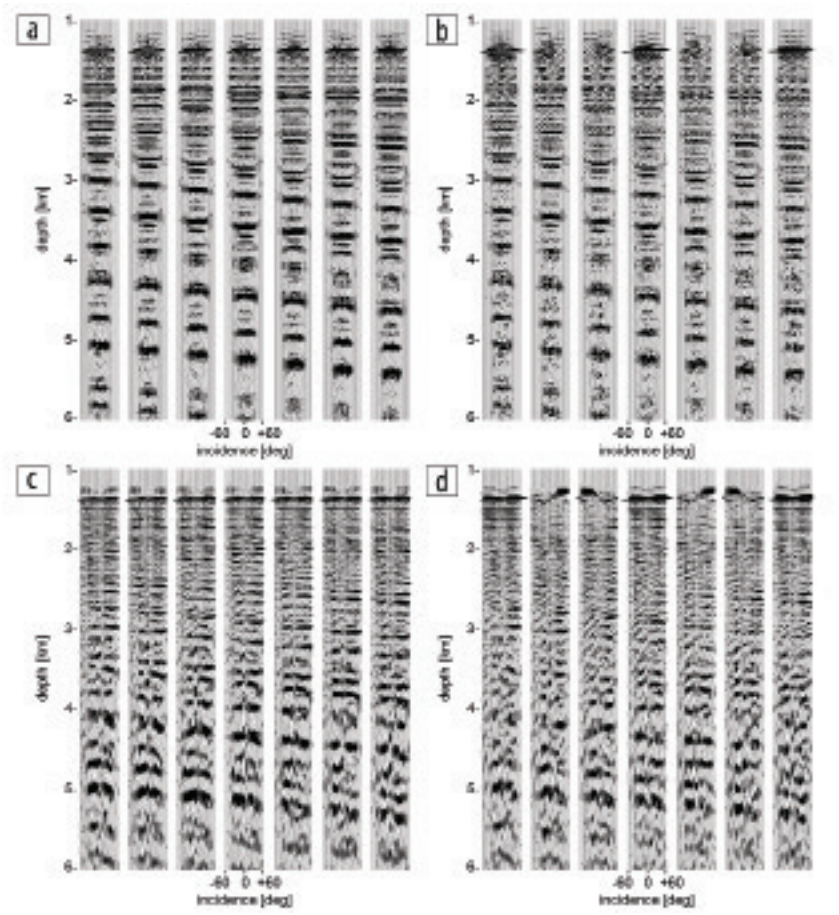

Figure 4. OBN 2D synthetic image-domain incidence-angle gathers after (a and b) PP-wave and (c and d) PS-wave migration, with receiver spacing of (a and c) 100 m and (b and d) 300 m.

Therefore, for different reasons, PP and PS CIGs from OBN geometry, either offset- or angle-indexed, are of limited use for global reflection tomography just below the seafloor when receiver spacing is large compared with P- and S-wave seismic wavelengths. The situation improves dramatically when receiver spacing is reduced to 100 m (Figures 4a and 4c).

Next, we show dip-angle gathers for PP and PS migration in Figure 5. The dip-angle range for both PP and PS is –45° to 45° with a 2°-angle bin sampling. Decomposing migrated images according to the local dip-angle domain (Ravve and Koren, 2011) has proved to be of practical use for illumination analysis in asymptotic (Audebert et al., 2002) and full-wavefield imaging (Li et al., 2012).

Another use of these gathers is to discriminate between continuous reflectors and diffractors in the subsurface (Landa et al., 2008). If an event on a dip-angle gather is coherent (flat or locally linear) over a small range of dips, we can be confident that it is a specular reflection from a continuous reflector. On the other hand, if an event is nearly linear over a wide range of dips, we can be confident that it is from a subsurface diffractor, which is built of components from a wide range of dips.

Here, PP and PS dip-angle CIGs for 100-m and 300-m receiver spacings all tell a similar story. The shallowest event (seafloor) is spread over a range of dips. Because of the wide receiver separation and the seismic wavelengths involved, virtually no seismic energy that reflected just below the seafloor has encountered adjacent receiver locations. That is, the receiver locations are imaged separately from one another, as if they are diffractors.

The same is true for the shallowest subseafloor reflectors in the PS migration. Although the migration's "interpretation" of these events is incorrect, it is consistent with the limitations imposed by the acquisition geometry. In the high-amplitude stratigraphic section (intermediate depths), both PP and PS CIGs have energy spread over a restricted (but not tiny) dip range.

This section has a dominant layering with many subtle features such as pinch-outs with low-amplitude diffraction signatures. The diffractions broaden the dip-angle range of energy in the CIGs, but their amplitudes are dominated by layering effects. In the deep section, energy on the PP and PS gathers is more localized, indicating some combination of dominant layering effects and loss of seismic resolution, with attenuation contributing to the latter.

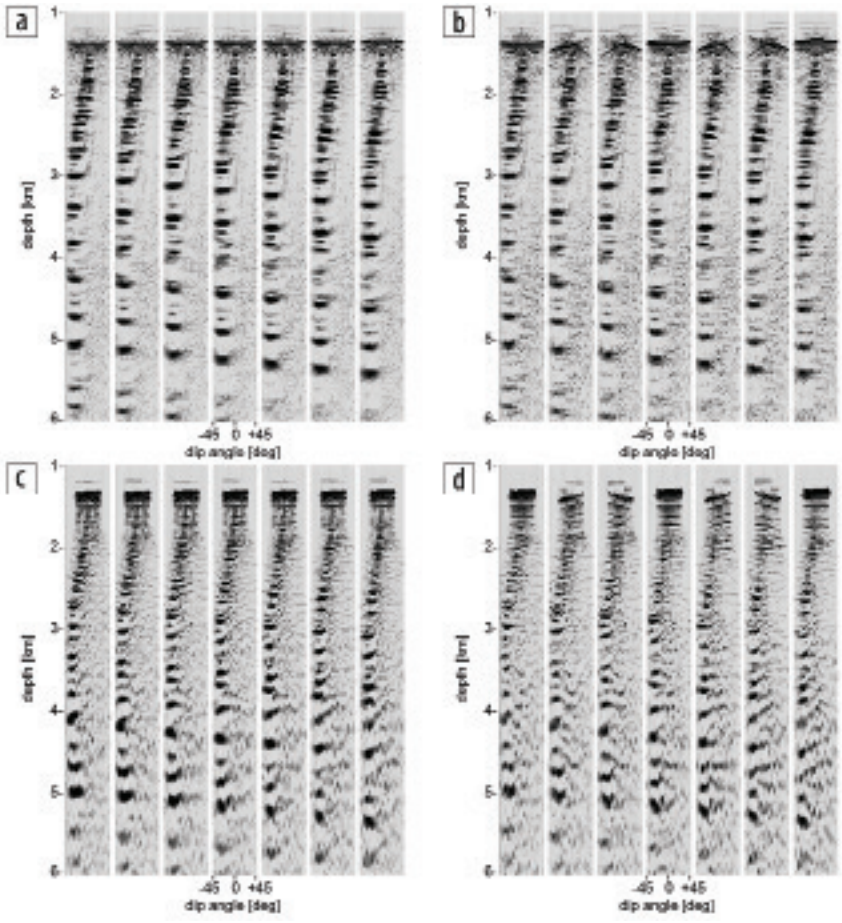

Figure 5. OBN 2D synthetic image-domain dip-angle gathers after (a and b) PP-wave and (c and d) PS-wave migration, with receiver spacing of (a and c) 100 m and (b and d) 300 m.

In general, isolated strong diffractors are relatively rare, and an incoherent spread of energy over a range of dip angles usually indicates many weak diffractors. The relative rarity of strong diffractors, for which upward or downward curvature indicates velocity error, limits the usefulness of diffractors for velocity analysis.

Some but not all dip-angle gathers for this survey show upward curvature on events, which is characteristic of specular reflections. In fact, reflector signatures in dip-angle gathers can have large curvature, even in the case of accurate migration models (Landa et al., 2008). These curved reflection events on dip-angle gathers usually need a finer angular sampling for detectability than the 2° sampling shown in Figure 5. In fact, a coarse angular spacing in dip-angle gathers can lead to aliasing noise in the gathers when the steep limbs of upward-curving events are sampled inadequately.

PS model building

Ray tomography based on residual curvature analysis in offset or angle CIGs is used widely to estimate a long-wavelength velocity field suitable for migration or as a starting guess for full-waveform-inversion model updates. The success of such inversion schemes relies on (1) signal-to-noise (S/N) ratio and density of the residual-moveout (RMO) picks and (2) the relative sensitivity of RMO to the model perturbation.

For streamer P-wave acquisition, the picked RMO curves are usually sufficiently dense, clean, and diagnostic, guaranteeing convergence toward a velocity model that minimizes the total RMO. Moreover, additional nonseismic data constraints (e.g., check shots, VSPs, well markers), along with a priori model statistics (e.g., directional smoothness and rock-physics information), often can resolve the velocity/anisotropy ambiguity at small incidence angles (Thomsen parameter δ) and produce geologically plausible models with small misties from interpreted formations at well locations.

For PP-wave OBC or OBN deepwater seafloor acquisitions, similar results can be obtained by performing two migrations, one with receivers at seafloor locations and the other with receivers at mirror locations. Just below the seafloor, the CIGs from the second migration will compensate the lack of velocity resolution in the CIGs from the first migration. In addition, including PS CIGs in a joint PP-PS tomographic inversion introduces extra constraints that can help in estimating accurate large-angle (Thomsen parameter ε) anisotropy models.

In practice, however, two factors challenge our ability to exploit PS CIGs from deepwater seafloor data — receiver undersampling and strong PS-wave propagation asymmetry. As illustrated in Figure 4d, the former makes the RMO picking incomplete and prone to error in CIGs. The latter affects RMO curve sensitivity to model parameters, in particular when updates of S-wave velocity V_S and anisotropy ε are needed at shallow depths. The following sensitivity analyses illustrate these problems.

Figure 6a shows a pair of PS stacked images using the OBN data set (receiver spacing 300 m), migrated with an incorrect velocity. Specifically, V_S was perturbed between the seafloor (red line) and a horizon 250 m below the seafloor (yellow line). The figure compares migration results using a V_S profile whose values were 10% lower (left side) and 10% higher (right side) than the correct values used in Figure 3d. The incidence-angle CIGs shown in Figure 6b are extracted from locations near the marked central location (vertical white line) in Figure 6a, and they illustrate the residual curvature induced by a lower (left) and higher (right) V_S model. Neither is the stacked image obviously defocused relative to the "correct" image in Figure 3d nor do the CIGs present any distinctive smiling/frowning pattern.

Reflection tomography, therefore, will not be sensitive to these velocity errors. In fact, given the deepwater location of the receiver, the total propagation time is dominated by the P-wave leg in the water. However, both the stack and CIGs clearly show vertical

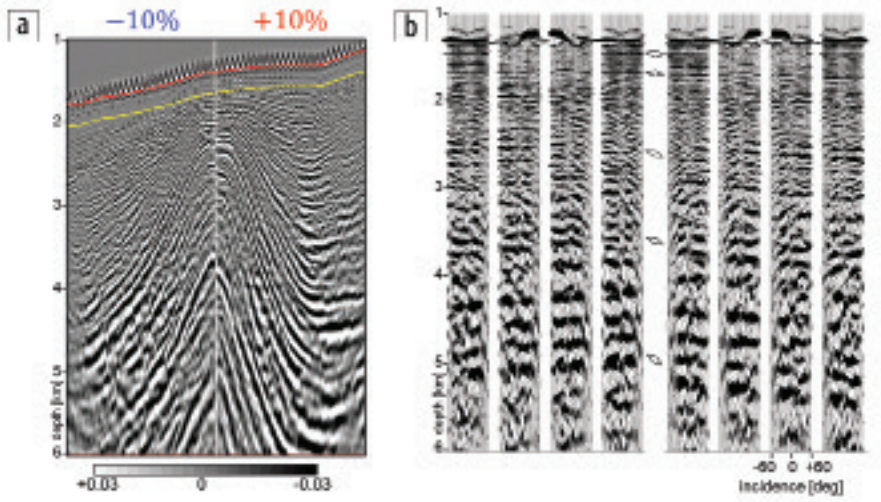

Figure 6. PS-wave imaging V_S sensitivity test. The correct V_S model is perturbed by ± 10% between the seafloor (red line) and a 250-m-deep horizon 250 m below the seafloor (yellow line). (a) Stacked image with –10% (left from the white vertical line) and +10% (right from the white vertical line) V_S. (b) Incidence-angle CIGs from the central location (white line in part [a]) with –10% (left) and +10% (right) V_S. The altered V_S field is mainly responsible for vertical mispositioning of the events. No clear residual RMO shows in the CIGs.

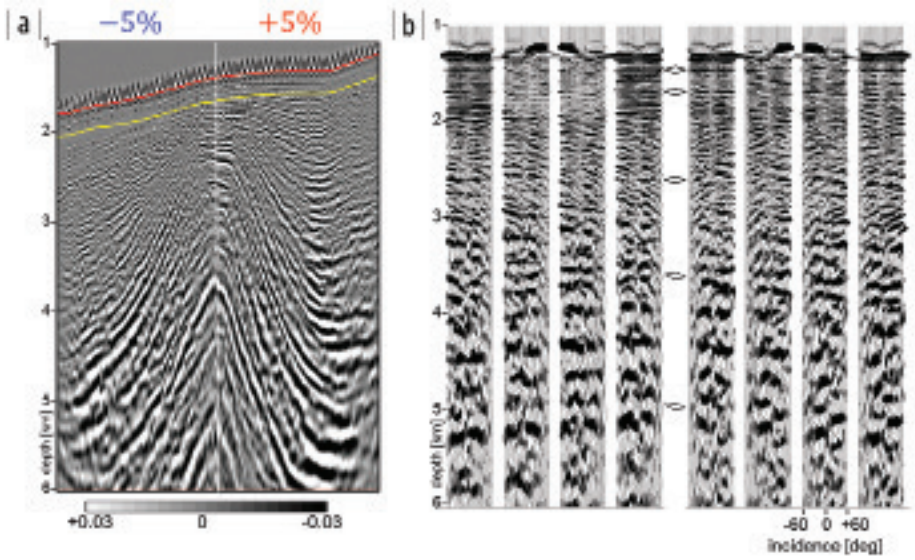

Figure 7. PS-wave imaging ε sensitivity test. The correct ε model is perturbed by ± .05 between the seafloor (red line) and a 250-m-deep horizon 250 m below the seafloor (yellow line). (a) Stacked image with –.05 (left from the white vertical line) and +.05 (right from the white vertical line) ε. (b) Incidence-angle CIGs from the central location (white line in part [a]) with –.05 (left) and +.05 (right) ε. The altered ε field is responsible for mispositioning and defocusing of the migrated events. Residual RMO is observable in the CIGs at middepths, where aliasing effects caused by sparse receiver sampling are reduced.

mispositioning from top to bottom. This is because the low S-wave velocity near the seafloor (300 m/s) tends to turn reflected PS energy nearly vertical at shallow depths. Therefore, especially near the seafloor, the problem of estimating S-wave velocity from deepwater recording resembles the problem of estimating near-surface statics typical of onshore surveys. (Deeper, reflection tomography is helpful, but not as much as in estimating P-wave velocity.)

The success of statics estimation relies on our ability to interpret and relate horizons on both the PP and PS images — so-called event registration. V_S then is obtained by imposing a 1D vertical codepthing constraint and inversion. In complex geology, a ray-based solution (D'Afonseca et al., 2014) can obtain a more plausible V_S field by imposing codepthing in a 3D sense. In addition, a 3D displacement field that describes the relative shifts between events on the PP and PS CIGs can be incorporated as an additional constraint into a tomographic inversion (Mathewson et al., 2013). When near-seafloor horizons cannot be interpreted from images obtained from sparse (or even dense) OBN acquisitions, estimating V_S becomes the dominant challenge in PS imaging.

Analogous to Figure 6, Figure 7 illustrates the effects of using an incorrect anisotropy profile. The figure compares migrated stack (Figure 7a) and incidence-angle CIGs (Figure 7b) with (left) .05 subtracted from and (right) .05 added to the correct Thomsen parameter ε profile, whose value in the shallow sediments is zero. These values correspond to lower and higher velocities at large incidence angles.

In this case, the perturbed anisotropy field produces images which are both laterally mispositioned and defocused (particularly in the core of the anticlinal feature at depths greater than 5 km). The higher sensitivity to perturbation in ε than to V_S relates to the asymmetry in PS-wave propagation.

The combination of Snell's law for PS reflection and lower S-wave velocity effectively forces the incident P-waves to travel at larger incidence angles. This effect is quantified by the presence of seismic energy at the larger incidence-angle bins (~ 60° in Figures 4c and 4d) in the PS CIGs than in the PP CIGs (~ 40° in Figures 4a and 4b). Defocusing is caused by a residual sloping up (Figure 7b, left) and down (Figure 7b, right) of energy in the CIGs, resulting in amplitude cancellation after stack.

These slopes, supplied to a joint PP-PS inversion with codepthing constraints (D'Afonseca et al., 2014), can produce an anisotropy update that will result in better PP and PS images. Moreover, because of the asymmetric nature of PS propagation, stacks from opposite azimuthal directions can show image misalignments that can be used as additional constraints in a tomographic inversion. In general for sparse OBN acquisition, the incomplete, aliased RMO information available near the seafloor makes tomographic inversion for the anisotropy field difficult and uncertain, and stack optimization using ε scans are

often preferable to a tomographic inversion that relies on RMO (Haacke et al., 2014).

Conclusions

We have presented and illustrated some opportunities and some challenges of imaging data acquired on the seafloor. One opportunity is the prospect of greater resolution of PS imaging than PP imaging; another is the prospect of additional PS information contributing to quantitative interpretation. Chief among challenges, tending to negate the opportunities, is the image degradation caused by large spacing of receivers on the seafloor. When receiver spacing exceeds an S-wavelength, PS migration has difficulty combining information from different receivers, essentially producing single-fold (or zero-fold) images just below seafloor.

In addition, when receiver spacing is large, even PP imaging potentially suffers from migration aliasing. Although we have not illustrated this, antialiasing should be applied carefully to seafloor PP and PS migrations. Otherwise, the result can be decreased lateral resolution, both in imaging and in velocity estimation.

We also have presented and described types of CIG available to seafloor data migrations. Information from these can be used in offset- or incidence-angle tomography. The success of tomographic inversion relies on (1) S/N and density of the residual-moveout picks and (2) their relative sensitivity to the model perturbation. PS CIGs from sparse deepwater acquisition do not fully meet these criteria because of aliasing and strong asymmetry in the PS-wave recording. This makes the task of PS-velocity model building an outstanding and challenging problem for deepwater OBN acquisition.

If the receiver interval is small enough, the offset- or incidence-angle-indexed CIGs also can be used in migration amplitude studies, particularly when PP and PS CIGs are analyzed together for lithology discrimination. Dip-angle CIGs are also available; the information carried in those gathers is subtle and requires care in extracting reliable estimates of diffractor locations.

Seafloor acquisition has the advantages over streamer acquisition in being closer to the reservoir and providing two wavefields for analysis. The first advantage (closer to the reservoir) becomes a disadvantage, however, when receivers are widely separated — a disadvantage that is mitigated for PP waves with mirror imaging but not for PS waves.

Wavefield sampling problems that are, in principle, serious for streamer data with widely spaced shots can be resolved to some degree in deep water simply by wavefront healing that occurs in propagation through the water column. For seafloor acquisition and nonmirror imaging, the luxury of wavefront healing is unavailable. Therefore, it is important to recognize that seafloor acquisition and combined PP and PS imaging can realize their full benefit only when the seafloor is well sampled with receivers, with an ideal spacing on the order of an S-wavelength or less. TLE

Acknowledgments

We thank Chevron for the use of the synthetic data set. We thank two reviewers for helpful comments.

Corresponding author: Sam.Gray@CGG.com

References

Amundsen, L., 2001, Elimination of free-surface related multiples without need of a source wavelet: Geophysics, **66**, no. 1, 327–341, http://dx.doi.org/10.1190/1.1444912.

Audebert, F., P. Froidevaux, H. Rakotoarisoa, and J. Svay-Lucas, 2002, Insights into migration in the angle domain: 72nd Annual International Meeting, SEG, Expanded Abstracts, 1188–1191, http:/dx.doi.org/10.1190/1.1816863.

Casasanta, L., and S. H. Gray, 2015, Converted-wave beam migration with sparse sources or receivers: Geophysical Prospecting, **63**, 1–18, http://dx.doi.org/ 10.1111/1365-2478.12226.

Gray, S. H., 2007, Angle gathers for Gaussian beam migration: 69th Conference and Exhibition, EAGE, Extended Abstracts, C018, http://dx.doi.org/10.3997/2214-4609.201401519.

Gray, S. H., 2013, Spatial sampling, migration aliasing, and migrated amplitudes: Geophysics, **78**, no. 3, S157–S164, http://dx.doi.org/10.1190/geo2012-0451.1.

D'Afonseca, L. A. D., M. Dumett, O. J. Birkeland, P. Guillaume, T. Krishnasamy, T. M. G. Santiago, and C. Guerra, 2014: S-ray approximation tomography for PP and PS horizon co-depthing: 76th Conference and Exhibition, EAGE, Extended Abstracts. http://dx.doi.org/10.3997/2214-4609.20140648.

Dash, R., G. Spence, R. Hyndman, S. Grion, Y. Wang, and S. Ronen, 2009, Wide-area imaging from OBS multiples: Geophysics, **74**, no. 6, Q41–Q47, http://dx.doi.org/10.1190/1.3223623.

Haacke, R. R., L. Casasanta, P. Chiarandini, N. V. V. Golla, A. Kalil, S. Drummie, I. Meades, and A. Strudley, 2014, PS-wave processing and velocity-model building from a sparse OBN array: 76th Conference and Exhibition, EAGE, Extended Abtracts, http://dx.doi.org/10.3997/2214-4609.20140649.

Hill, N. R., 2001, Prestack Gaussian-beam depth migration: Geophysics, **66**, no. 4, 1240–1250, http://dx.doi.org/10.1190/1.1487071.

Landa, E., S. Fomel, and M. Reshef, 2008, Separation, imaging, and velocity analysis of seismic diffractions using migrated dip-angle gathers: 78th Annual International Meeting, SEG, Expanded Abstracts, 2176–2180, http://dx.doi.org/10.1190/1.3059318.

Li, Z., B. Tang, and S. Ji, 2012, Subsalt illumination analysis using RTM 3D dip gathers: 82nd Annual International Meeting, SEG, Expanded Abstracts, http://dx.doi.org/10.1190/segam2012-1348.1.

Mathewson, J., M. Woodward, D. Nichols, C. Xu, and C. Leone, 2013, Joint PP/PS tomography with floating event constraints: 78th Annual International Meeting, SEG, Expanded Abstracts, 1649–1653, http://dx.doi.org/10.1190/segam2013-1444.1.

Ravve, I., and Z. Koren, 2011, Full-azimuth subsurface angle domain wavefield decomposition and imaging: Part 2 — Local angle domain: Geophysics, **76**, no. 2, S51–S64, http://dx.doi.org/10.1190/1.3549742.

Rosales, D., and J. Rickett, 2001, PS-wave polarity reversal in angle domain common-image gathers: 71st Annual International Meeting, SEG, Expanded Abstracts, 1843–1846, http://dx.doi.org/10.1190/1.1816489.

Stewart, R., J. Gaiser, J. Brown, and D. Lawton, 2003, Converted-wave seismic exploration: Applications: Geophysics, **68**, no. 1, 40–57, http://dx.doi.org/10.1190/1.1543193.

Wang, Y., S. Grion, and R. Bale, 2010, Up-down deconvolution in the presence of subsurface structure: 72nd Conference and Exhibition, EAGE, Extended Abstracts, D001, http://dx.doi.org/10.3997/2214-4609.201400704.

Xu, S., H. Chauris, G. Lambaré, and M. Noble, 2001, Common-angle migration: A strategy for imaging complex media: Geophysics, **66**, no. 6, 1877–1894, http://dx.doi.org/10.1190/1.1487131.